

## Dynamics of wetting: from inertial spreading to viscous imbibition

This article has been downloaded from IOPscience. Please scroll down to see the full text article.

2009 J. Phys.: Condens. Matter 21 464127

(<http://iopscience.iop.org/0953-8984/21/46/464127>)

View [the table of contents for this issue](#), or go to the [journal homepage](#) for more

Download details:

IP Address: 129.252.86.83

The article was downloaded on 30/05/2010 at 06:03

Please note that [terms and conditions apply](#).

# Dynamics of wetting: from inertial spreading to viscous imbibition

L Courbin<sup>1,2</sup>, J C Bird<sup>1</sup>, M Reyssat<sup>1</sup> and H A Stone<sup>1,3</sup>

<sup>1</sup> School of Engineering and Applied Sciences, Harvard University, Cambridge, MA 02138, USA

<sup>2</sup> IPR, UMR CNRS 6251, Campus Beaulieu, Université Rennes 1, 35042 Rennes, France

E-mail: [hastone@princeton.edu](mailto:hastone@princeton.edu)

Received 20 April 2009, in final form 9 July 2009

Published 29 October 2009

Online at [stacks.iop.org/JPhysCM/21/464127](http://stacks.iop.org/JPhysCM/21/464127)

## Abstract

We report the influence of the nature of boundaries on the dynamics of wetting. We review some work recently published and highlight new experimental observations. Our paper begins with the spreading of drops on substrates and demonstrates how the exponents of the spreading laws are affected either by the surface chemistry or by the droplet shape. We then discuss the imbibition of completely and partially wetting fluids into channels and over microtextured surfaces. Starting with the one-dimensional imbibition of completely wetting liquids in tubes and surface textures, we show that (i) shape variations of channels change the power-law response of the imbibition and (ii) the geometrical parameters of a surface roughness change the spreading behavior. For partially wetting fluids, we observe directionally dependent spreading: polygonal wetted domains can be obtained. We conclude with a tabular summary of our findings, allowing us to draw connections between the different systems investigated, and shed light on open questions that remain to be addressed.

(Some figures in this article are in colour only in the electronic version)

## 1. Introduction

When a liquid makes contact with any surface, the contact line moves until the liquid/solid/vapor system reaches equilibrium state. The dynamics on how the liquid reaches its equilibrium are not trivial and vary with surface chemistry, surface topography, and liquid properties [1–4]. In this contribution, we focus on systems where the dominant driving force results from the reduction of surface energy, i.e. the capillary force. Specifically, we report on the wetting dynamics for different liquid–solid systems.

For ideal surfaces (i.e. smooth and chemically homogeneous), a minimization of the variation of the total surface energy needed to move the contact line a distance  $dx$  (see figure 1(a)) leads to the familiar Young's relation that defines the equilibrium contact angle  $\theta_{\text{eq}}$  formed between the drop and the substrate:  $\cos \theta_{\text{eq}} = (\gamma_{\text{sv}} - \gamma_{\text{sl}})/\gamma$  [3]. In this relation,  $\gamma_{\text{sv}}$ ,  $\gamma_{\text{sl}}$  and  $\gamma$  denote, respectively, the solid/vapor, solid/liquid and liquid/vapor surface tensions (i.e. energy per unit surface area). Therefore if one of the phases is air, there are two ways to vary

$\theta_{\text{eq}}$ ; either by changing the surface tension of the liquid,  $\gamma$ , or by modifying the surface chemistry.

Only ideal surfaces are smooth and it is well known that both surface chemistry and surface roughness affect the dynamics of wetting [6]. Understanding the influence on dynamics of wetting of surface chemistry or surface topography alone, or surface chemistry together with surface roughness, can yield new understanding and potential applications involving wetting, both statics and dynamics, for a large variety of situations, both in nature and in industry.

In the laboratory, we used soft-lithography methods to design and manufacture topographically patterned, but chemically homogeneous, surfaces made of polydimethylsiloxane (PDMS) [7]. Without further surface treatment, PDMS is hydrophobic so that a water droplet partially wets the surface with an equilibrium contact angle  $\theta_{\text{eq}} \approx 90^\circ$  (see figure 1(b)). We manufactured surface textures that consist of micron-size cylindrical posts arranged on a square lattice with post radii and heights,  $R$  and  $H$ , and lattice distances  $d$  (figure 1(c)). Figure 1(d) shows an example of the well known 'fakir' effect: the increase in surface area resulting from the addition of surface roughness to a smooth PDMS substrate makes it

<sup>3</sup> Present address: Department of Mechanical and Aerospace Engineering, Princeton University, Princeton, NJ 08544, USA.

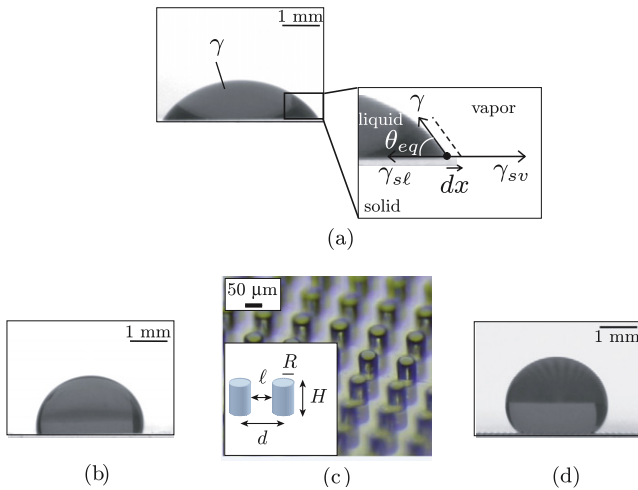


**Figure 1.** (a) Partial wetting of an ethanol droplet on a smooth PDMS substrate. Inset: close-up of the contact line the drop makes with the substrate showing Young's construction. (b) A drop of water deposited on smooth hydrophobic PDMS makes an equilibrium contact angle close to  $\theta_{eq} \approx 90^\circ$ . (c) Micropatterned surface made of PDMS and schematic depicting the topographical features. (d) A drop of water deposited on a rough PDMS (superhydrophobic) substrate (as shown in (c)) adopts a nearly spherical shape,  $\theta_{eq} \approx 150^\circ$ . The pictures of drops are adapted from [5].

superhydrophobic,  $\theta_{eq} \approx 150^\circ$ . In this 'fakir' state, a drop of water adopts a nearly spherical shape and easily rolls off the substrate [6, 8]. In contrast, complete wetting, i.e.  $\theta_{eq} \approx 0^\circ$ , can be achieved by using a droplet of oil that completely wets a smooth PDMS substrate.

Here we discuss the influence of boundary conditions on the dynamics of wetting of drops on smooth surfaces, and moving liquid fronts in smooth tubes and microtextured substrates. We begin in section 2 by describing the dependence of the spreading dynamics of drops on  $\theta_{eq}$  and on the shape of the drop; our focus is on short times where we find a dominant influence of inertia. Next, we discuss one-dimensional viscous imbibition of completely wetting fluids in tubes and microtextured surfaces (sections 3). We show that variations in the tube cross-sectional area affect the long-time imbibition dynamics. In the case of surface roughness, we discuss the role of the topographic features on the motion of the liquid front in the porosity. In section 4, we demonstrate that directionally dependent spreading can be achieved during the imbibition of partially wetting fluids on rough surfaces and that a polygonal wetted area can be obtained. The three distinct themes of this paper, drop spreading, one-dimensional imbibition, and two-dimensional wicking of textures, are represented in a schematic shown in figure 2. Our paper focuses on three controls, the shape of the boundary, the equilibrium contact angle, and the surface roughness, which are inherent to the central theme, wetting dynamics (figure 2).

## 2. Inertial imbibition: the early time dynamics of wetting

In this section we describe the dynamics of a liquid drop as it contacts and subsequently wets a solid surface. We

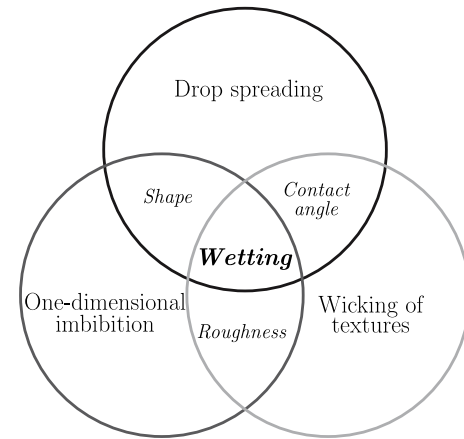


**Figure 2.** Schematic representing the different aspects of wetting we discuss in this paper: drop spreading, one-dimensional imbibition, and wicking of textures. The intersections of the circles emphasize the connections that exist between topics: the shape of a boundary matters for drop spreading and one-dimensional imbibition, the equilibrium contact angle affects the dynamics of droplets and wicking of surface textures, and both one- and two-dimensional imbibition of microtextured surfaces are influenced by the topographic features of a surface roughness. Wetting is the central theme of these areas.

begin by reviewing how a drop spreads on a dry, completely wetting surface (equilibrium contact angle  $\theta_{eq} = 0^\circ$ ). Next, we describe how the early wetting behavior is modified when the surface is partially wetting ( $\theta_{eq} > 0^\circ$ ). This work on partial wetting adds a few additional details to our recent paper [9]. Finally, we share new observations and analytical considerations for the influence of the initial drop shape on the early time spreading dynamics. In particular, by applying an electrical potential across the drop, we are able to change the shape of the drop from spherical to conical prior to contact with the surface. Immediately after contact, both conical and spherical drops spread out; however, the spreading dynamics in the two cases follow different power-law scalings.

### 2.1. Complete wetting

When a drop of completely wetting liquid contacts a smooth and dry surface, the drop spreads along the surface in order to minimize the total potential and surface energy. For small drops, whose radii are smaller than the capillary length, the effects of gravity are negligible and spreading is driven by capillary forces. Figure 3 illustrates via high-speed video images the dynamics when a water drop contacts a completely wetting solid. The images show two distinct wetting regimes. At early times (figures 3(a)–(c)), the surface of the drop significantly deforms as a capillary wave travels along the surface of the drop. In this regime the capillary forces due to the curved surface rapidly drive the spreading process while the inertia of the fluid resists the deformation [9, 10].

Once the capillary waves have dissipated, the spreading liquid enters into a second stage of wetting (figures 3(f)–(h)). In this second regime, the drop continues to spread, but at a significantly slower rate. Here the spreading drop takes the form of a spherical cap with a small dynamic contact angle,

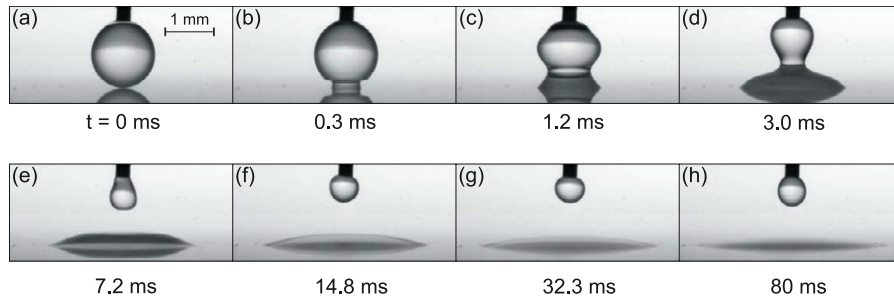


**Figure 3.** A drop of water rapidly spreads upon contacting a completely wetting surface (here a plasma-treated glass slide).

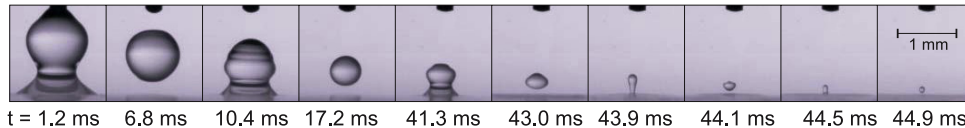


**Figure 4.** Drops spreading on wet or dry, completely wetting surfaces can partially coalesce forming a smaller drop that itself exhibits similar coalescence dynamics. The resulting cascade continues until the ejected drop is small enough that viscous effects change the dynamics. Here a water drop progresses through five iterations before fully coalescing with the thin water film.

and the surface energy gained by spreading is balanced by the viscous dissipation associated with this motion [3, 11].

Between the two regimes (figures 3(d) and (e)), the amplitude of the surface deformation is large enough to separate the drop into two parts. One part remains suspended by the needle and retracts to form a sphere, and the other part continues to spread on the surface. This phenomenon is often referred to as partial coalescence (only part of the drop coalesces with the surface) so as not to be confused with partial wetting, which refers to the dynamics that occur when a drop contacts a solid with a finite contact angle.

If the separated drop breaks free of the needle, or simply exists in the absence of a needle, the separated smaller drop falls to the interface where it begins to coalesce with the wetted surface (figure 4). During the coalescence another smaller drop pinches off setting up a cascade of partial coalescence, as investigated by [12, 13]. Viscosity suppresses this partial coalescence when the Ohnesorge number is sufficiently large,  $\mu/(\rho\sigma R)^{1/2} > 0.026$  [13]. After five iterations, the size of the ejected drop in figure 4 is small enough that it fully coalesces, ending the cascade. Here we have shown that this coalescence cascade occurs even when only a thin wetting film on a substrate exists, whereas early work had focused on coalescence with a deep bath of liquid. This observation emphasizes that the dynamics are controlled by inertia of the droplet liquid.

Figures 3 and 4 also demonstrate the similarity between the dynamics of a drop spreading on a dry, completely wetting surface and spreading on a wet surface. Experiments have demonstrated that on completely wetting surfaces a microscopic film precedes the macroscopic advancing contact line [3, 14]. This precursor film may explain why spreading on dry, completely wetting surface is similar to spreading on a pre-wet surface; in both cases the drop coalesces with a thin film [10]. However when a drop contacts a dry, partially wetting surface ( $\theta_{eq} > 0$ ), coalescence arguments

are no longer appropriate, and instead contact line dynamics (e.g. surface energies associated with all three phases) need to be considered.

## 2.2. Partial wetting

As a spherical drop begins to spread on a dry, partial wetting surface, there are three different interfaces that intersect to form a contact line. Since viscous stresses diverge near the contact line [15], it might be expected that the capillary spreading is regulated solely by viscous dissipation. However, recent work by our group has shown that this is not the case [9].

In order to study the early time dynamics we used water-glycerol mixtures and modified silicon surfaces using standard surface chemistry techniques [3, 9]. The liquid is slowly extruded through the end of a hydrophobic needle to form a growing pendant drop. As long as the size of the drop is well below the capillary length, the drop remains nearly spherical until contact. We observe a striking difference in the spreading behavior depending on the surface; typical experimental results are shown in figure 5. Similar results have also been reported in [16]. When drops are placed on a hydrophilic surface, the liquid rapidly wets the surface and forms an acute dynamic contact angle (top row in figure 5). However when the drops are placed on a hydrophobic surface, the spreading liquid wets the surface slow enough to form an obtuse dynamic contact angle (third row in figure 5). To better understand the dynamics, we vary the fluid dynamic viscosity,  $\mu$ , and the initial drop radius,  $R$ . We then try two scalings of the data: (i) inertial and (ii) viscous (figure 6).

Figure 6(a) reports how the wetted radius  $r$  grows with time  $t$  once a drop contacts one of the four surfaces shown in figure 5; results for many different drop radii and three different fluid viscosities are shown. The results reiterate that the drop-spreading speed increases as the equilibrium contact angle of the surface decreases. The plot also reveals that larger

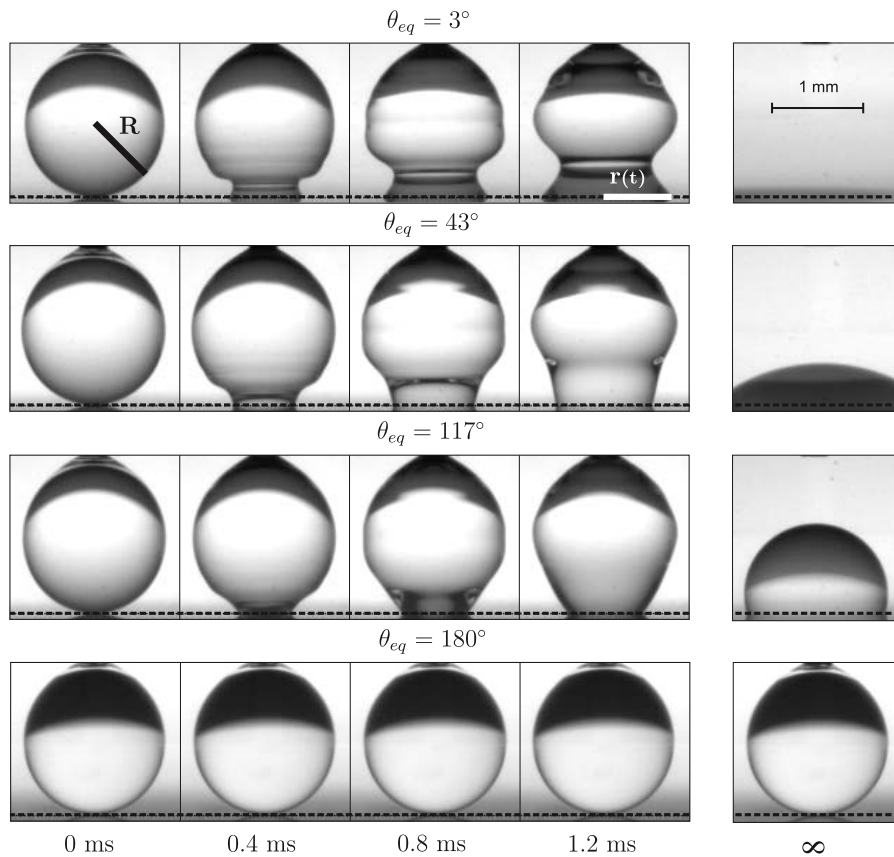


**Figure 5.** The early time spreading of water drops on partially wetting surfaces, where the contact angle is indicated in each figure. The final images in each column shows the shape of the drops after a minute, which we assume to be near equilibrium. Figure adapted from [9].

drops spread faster than smaller drops on each of the surfaces. Changing the viscosity of the fluid by a factor of ten has a relatively small effect on the spreading rate with the more viscous drops tending to spread slower than the less viscous drops.

We can better characterize the spreading behavior by non-dimensionalizing the data in figure 6(a). The natural length scale in this problem is the initial radius of the drop  $R$ . Yet there are two possible timescales to consider. If the capillary forces driving the flow are primarily hindered by viscosity, then the natural timescale is  $\mu R/\gamma$ , where  $\gamma$  is the interfacial tension between the liquid and surrounding gas. However, if inertia of the liquid is the primary hindrance, then the natural timescale is  $(\rho R^3/\gamma)^{1/2}$ , where  $\rho$  is the density of the liquid. Figures 6(b) and (c) shows how the results in figure 6(a) are rescaled with these natural timescales.

The data rescaled with the viscous timescale (figure 6(b)) further separates the results indicating that the spreading in figure 5 is not viscously dominated. Meanwhile the data rescaled with the inertial timescale (figure 6(c)) nearly collapses onto four master curves, each corresponding to a different equilibrium contact angle. The implication is that the early moments of spreading on partially wetting fluids can be inertially dominated, even when there is a distinct moving contact line. The rescaling in figure 6(c) also shows that smaller drops spread faster than larger drops relative to their

initial size even though larger drops spread faster than smaller drops on each of the surfaces in absolute terms.

While figure 6 clearly demonstrates that inertia is primarily responsible for regulating the speed of the capillary-driven wetting, it is necessary to further investigate the master curves to better understand the physical mechanism. When two drops coalesce, or when one drop spreads on a completely wetting substrate, the spreading radius in the inertial regime has a power-law dependence on time,  $r \propto t^{1/2}$ . Therefore it is natural to investigate whether the partial wetting results also follow a power-law behavior. As the master curves in figure 6 show, not only do the results of  $r$  versus time follow a power-law behavior, but the exponent appears to depend on the equilibrium contact angle (figure 7).

We find that spreading on partially wetting surfaces follows the power-law  $r/R = C(t/\tau)^\alpha$ , where  $\tau = (\rho R^3/\gamma)^{1/2}$  is the inertial timescale and  $\alpha$  is an exponent that depends on the equilibrium contact angle (figure 7). For small contact angles,  $\alpha$  approaches a value of 1/2, a value also observed for complete wetting and coalescence. Yet for larger contact angles,  $\alpha$  decreases continuously so that it reaches a value near 1/4 when the contact angle is approximately 117°.

In our recent work we proposed that this initial stage of spreading is regulated by the generation of capillary waves, similar to the analysis of planar wedges by [17, 18]. The resulting scaling analysis recovers the dynamic wetting



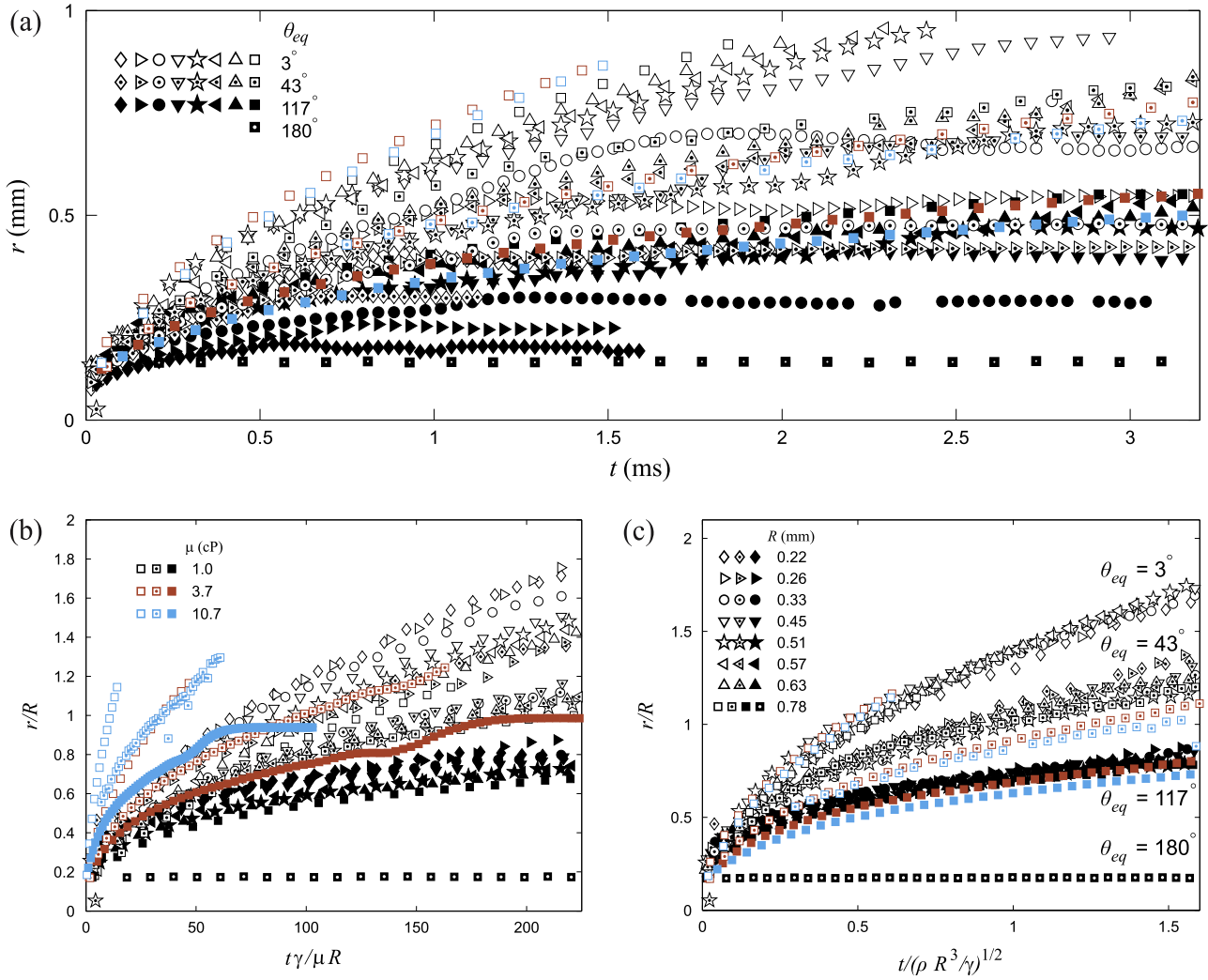


**Figure 6.** (a) The distance a drop spreads over time depends on the surface chemistry (symbol filling), viscosity (symbol color), and the initial drop size (symbol shape) as delineated in the legends for parts (b) and (c). (b) Rescaling the data with the viscous timescale spreads out the data points, whereas (c) rescaling the data with the inertia timescale approximately collapses the data onto four master curves each corresponding to a different equilibrium contact angle. Figure adapted from [9].

behavior  $r/R = C(t/\tau)^\alpha$  with  $\alpha = C_1 \sqrt{F(\theta_{eq}) + \cos \theta_{eq}}$ . Here  $C_1$  is a proportionality constant and  $F(\theta_{eq})$  is an unknown function that only weakly depends on  $\theta_{eq}$  [9]. The scaling provides no additional insight into why completely wetting drops spread with an exponent  $\alpha = 1/2$ , as a more detailed analysis would be required to predict the values of the constants. However, the result is successful in demonstrating how the equilibrium contact angle is able to affect spreading power  $\alpha$ .

In section 2.3, we return to completely wetting conditions and investigate how the initial *shape* of the drop influences the spreading dynamics.

### 2.3. Shape matters

To the best of our knowledge, previous drop-spreading experiments have only considered nearly spherical drop shapes. Yet, conical drops are surprisingly ubiquitous and occur naturally when there are electrical charge differences

between the drop and substrate. We investigate the effects of the voltage difference on the drop shape and subsequent wetting dynamics through an experiment similar to those described in the previous two sections.

A stainless steel needle is positioned 1–2 mm above a glass slide that acted as our target substrate. The glass slide is rinsed with ethanol, dried with nitrogen gas, and plasma treated within minutes of the experiments to ensure that the surface was completely wetting. Both the needle and the slide are connected to a voltage source so that the voltage across the gap can be controlled. Water is injected slowly through the needle to form a growing pendant drop which eventually contacts the slide (figure 8). Experiments were conducted with either no applied potential, in which case both the needle and the slide were grounded, or with a 500 V potential difference. These experiments were repeated on a thin layer of water coating the glass slide.

We observe that a potential difference across the drop significantly modifies the drop shape as it contacts the substrate

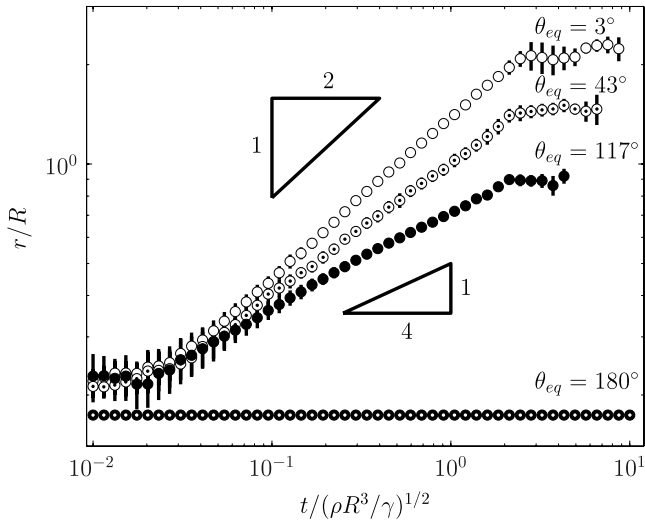


**Figure 7.** The master curves in figure 6(c) obey a power-law response where the exponent depends on the equilibrium contact angle. Vertical lines denote two standard errors. To prevent any bias from viscosity, only the data for  $\mu = 1$  cP was included in the average; the influence of viscosity on the coefficient of the power law is reported in [9]. Figure adapted from [9].

(e.g. contrast figures 8(a) and (b), 8(c) and (d)). When both the needle and slide are grounded, the drop remained spherical as water is injected through the needle. However in the presence of a 500 V potential difference, the drop begins spherical but then reaches a critical size and deforms into a cone (figure 8). Electrocapillary instabilities have been studied extensively [19], and conical deformations are often observed [20, 21]. Yet, the spreading dynamics after an electrically deformed drop contacts a solid or liquid have not been studied to the best of our knowledge. The electrical permittivity of water is approximately  $\epsilon = 7 \times 10^{-12}$  F m<sup>-1</sup>, and a typical conductivity is around  $\sigma = 5 \times 10^{-4}$  S m<sup>-1</sup>. If we assume that upon contact electrical charges equilibrate at the charge relaxation timescale  $\epsilon/\sigma$ , then following contact the system would be effectively neutralized within microseconds. Since our experiments are on the order of *milliseconds*, we neglect charge and instead focus on the shape of the interface following contact.

The spreading dynamics for the drops shown in figure 8 are plotted in figure 9. There is a striking difference in

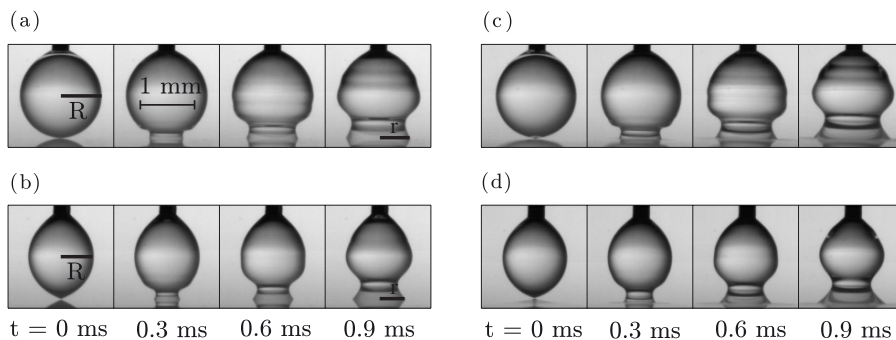


**Figure 8.** The early time spreading of spherical and conical drops on both dry and wet surfaces. The shape of the drop is controlled by varying the electrical potential difference across the drop. (a) Spherical on dry surface. (b) Conical on dry surface. (c) Spherical on wet surface. (d) Conical on wet surface.

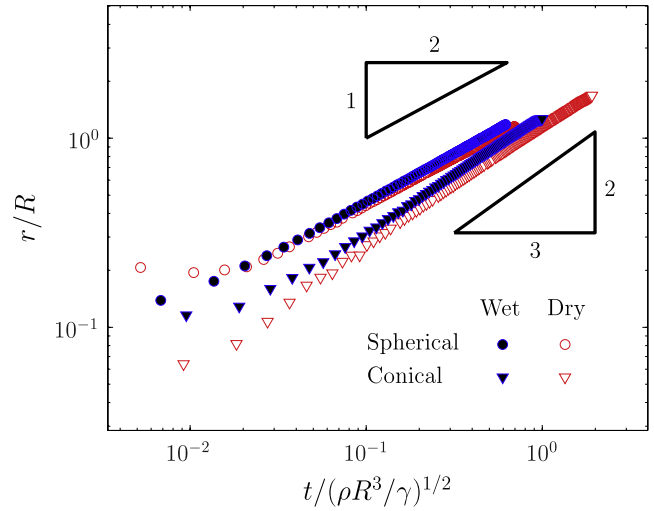


**Figure 9.** Experimental data on the spreading time for spherical and conical drops on both wet and dry surfaces.

the spreading behavior for initially spherical versus initially conical drops. The spreading of the spherical drops follow the expected power-law relation  $r/R \propto (t/\tau)^{1/2}$  where  $\tau = (\rho R^3/\gamma)^{1/2}$  is the characteristic inertial timescale. In contrast, the spreading of the conical drops appears to follow dynamics much closer to  $r/R \propto (t/\tau)^{2/3}$ . In other words, we find that the change in the initial drop shape effects the exponent of the power-law behavior, not just the prefactor.

In experiments in which the voltage was uncontrolled, we found that natural static charges often would deform the drop and lead to the 2/3 power-law exponent. These charge effects may be partially responsible for some of the variability between the spreading exponents reported in the literature, e.g. [10, 16].

In addition, the spreading dynamics on wet and dry surfaces are nearly identical for both geometries, suggesting that a coalescence model is appropriate in both situations. It has been suggested that when a spherical drop wets a completely wetting surface, the dynamics are identical to the drop coalescing with its precursor film [10] (section 2.1). A similar comparison may be appropriate for the dynamics of an initially conical drop.

Conical drops are unique in that they initially have zero curvature in the radial direction near the contact point. Therefore the initial spreading should be independent of the drop radius, and for dimensional reasons, it follows that in the absence of viscous effects conical drops should spread as  $r \propto (\gamma t / \rho)^{2/3}$ . Similar expressions have been deduced analytically for planar wedges of liquid coalescing [17]. Nonetheless, it is surprising that the spreading power law continues well beyond the initial conical region (figures 8 and 9).

Another approach to find the shape dependence on spreading is to generalize the existing inertially dominated spreading models [10, 22]. If we assume that the curvature of the growing meniscus is set by the gap between the drop and substrate  $z$ , then the capillary pressure driving the spreading scales as  $\gamma/z(r)$ , where the height  $z(r)$  depends on the radial position of the meniscus  $r$ . Here we assume that the negative curvature along the meniscus is greater than the positive curvature around the meniscus. Since viscous effects are neglected, the dynamics are expressed with the Euler equations, suggesting that the capillary pressure  $\gamma/z(r)$  ought to be the same order of magnitude as  $\rho(\partial_t r)^2$ , where  $\partial_t$  denotes a time derivative. This balance yields the following estimate for the spreading distance

$$r^2 z(r) \propto \frac{\gamma}{\rho} t^2. \quad (1)$$

If the shape of the drop at contact is expressed in the form  $z/R \approx (r/R)^\beta$ , then the predicted spreading rate would follow

$$r \propto \left( \frac{\gamma R^{\beta-1}}{\rho} \right)^{1/(\beta+2)} t^{2/(\beta+2)}, \quad (2)$$

which can be expressed in non-dimensional terms as

$$\frac{r}{R} \propto \left( \frac{t}{\tau} \right)^{2/(\beta+2)}, \quad (3)$$

where  $\tau = (\rho R^3 / \gamma)^{1/2}$  is the characteristic inertial timescale.

For a spherical drop, the shape can be approximated as parabolic near the contact point. Immediately after contact, the shape of the spreading drop is perturbed within the meniscus, but appears stationary outside this region such that  $\beta = 2$ . With this value of  $\beta$ , the spreading law follows the experimentally observed form  $r/R \propto (t/\tau)^{1/2}$ . For a conical drop,  $r \propto z$  such that  $\beta = 1$ . With this value of  $\beta$ , the predicted spreading law changes to  $r/R \propto (t/\tau)^{2/3}$ .

Here we have discussed the influence of the shape of the drop on the dynamics of spreading. Similarly, the shape of fixed boundary conditions, such as the walls of a capillary tube can also affect the exponents of spreading power laws. Such effects are discussed in section 3.

### 3. One-dimensional viscous imbibition

#### 3.1. Traditional imbibition

We now discuss the situation of one-dimensional viscous wetting and are focusing on the long-time viscous dynamics. In that situation, the inertial early time imbibition [23] is not

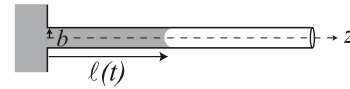


**Figure 10.** Capillary tube (of radius  $b$ ) brought into contact with a wetting liquid: spontaneous imbibition takes place inside the tube. Here  $\ell$  denotes the position of the meniscus at the time  $t$ .

observed and the viscous dissipation at the contact line [24] is negligible. Let us start with the classical configuration where a capillary cylindrical tube (of radius  $b$ ) is brought into contact with a wetting liquid of surface tension  $\gamma$  and dynamic viscosity  $\mu$  (see figure 10). Spontaneous imbibition takes place inside the tube to minimize energy. The motion of the fluid can be described by the Darcy's equation, which balances the viscous friction against the pressure gradient that drives the fluid:

$$\frac{\mu u}{k} = -\frac{\partial p}{\partial z}, \quad (4)$$

where  $u(z, t)$  is the average velocity of the liquid and  $k$  is the permeability of the tube ( $k = b^2/8$ ). The pressure gradient is given by the Laplace pressure at the meniscus over the length  $\ell$  ( $\frac{\partial p}{\partial z} = -\frac{2\gamma \cos \theta_{\text{eq}}}{b\ell}$ ) where  $\theta_{\text{eq}}$  is the equilibrium contact angle on the solid. Taking into account that  $u = d\ell/dt$ , the Darcy's equation leads to the classical result, often called the Washburn law [25] or the Lucas–Washburn law [26], which stipulates that the position of the meniscus increases as the square root of time  $\ell = \sqrt{Dt}$ , where  $D = \frac{\gamma b \cos \theta_{\text{eq}}}{2\mu}$  is a function of the physical characteristic of the liquid and of the radius of the tube. The observation and explanation for  $\ell \propto t^{1/2}$  originates from a 1906 paper by Bell and Cameron [27]. This result is rather generic and applies to a wide range of porous homogeneous media, e.g. paper, sand, and so on [28], and can be extended to microfabricated materials as discussed in section 3.3 or to V-shaped open grooves [29, 30].

#### 3.2. Wicking within systems with axial variations of permeability

Recently, we have studied the influence of a variation of permeability on the imbibition dynamics [31]. The permeability was modified by considering tubes of non-uniform cross section. We demonstrated, experimentally and theoretically, that shape variations of the channel or tube, along the flow direction, modify the classical response generally observed. The analysis relies on a combination of a one-dimensional approximation using Darcy's law and mass conservation. The equations are completed by applying boundary conditions on the pressure both at the inlet (the reservoir) and the outlet (accounting for the capillary pressure reduction that wicks the fluid into the tube).

As an example, we studied in detail the case of imbibition in conical tubes defined by their initial radius  $b_0$  and their opening angle  $\alpha$  (see figure 11(a)). Liquids are characterized by their surface tension  $\gamma$  and their viscosity  $\mu$ , and we determined the progression of the meniscus position  $\ell$  inside the cones as a function of time  $t$ . The analysis leads to the definition of two dimensionless parameters, a length  $L =$



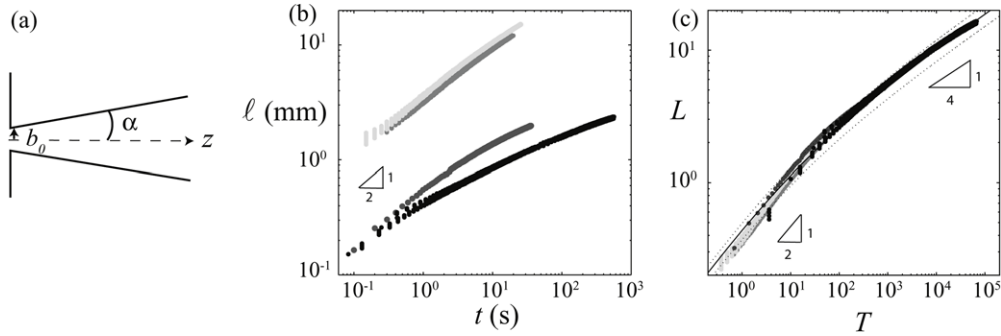


**Figure 11.** (a) A cone is defined by two parameters: its initial radius  $b_0$  and its opening angle  $\alpha$ . (b) Experimental results reported as a log–log plot of the position of the meniscus inside the cones as a function of time. Experiments have been performed with silicon oil of viscosity  $\mu = 0.1$  Pa s and surface tension  $\gamma = 2 \times 10^{-2}$  N m $^{-1}$  and realized on four different kinds of cones. The slope 1/2 represents the classical response for imbibition. (c) Rescaling of the data with the dimensionless parameters, length ( $L$ ) and time ( $T$ ), defined in the text. The continuous line corresponds to the polynomial solution:  $2L^4 + 8L^3 + 12L^2 = 3T$ . Two regimes are visible: at short times, the motion follows  $L \propto T^{1/2}$ , whereas at longer times, the motion is much slower and follows  $L \propto T^{1/4}$ . Figure adapted from [31].

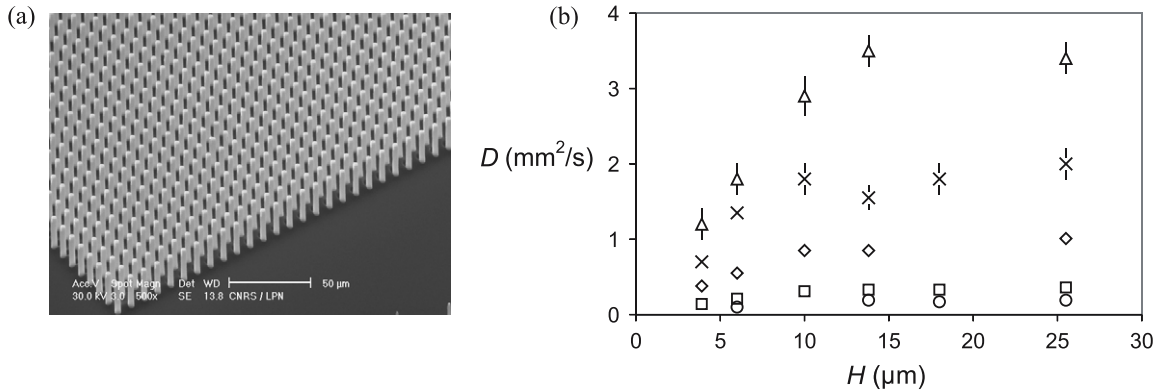


**Figure 12.** (a) Silicon surface decorated with a square pattern of micropillars (lattice spacing  $10 \mu\text{m}$ ). The bar indicates  $50 \mu\text{m}$ . (b) Dynamical coefficient of wicking  $D$  defined in the text as a function of the height  $H$  of the pillars expressed in micrometers. Oil viscosity is  $4.6$  mPa s ( $\Delta$ ),  $9.5$  mPa s ( $\times$ ),  $19$  mPa s ( $\diamond$ ),  $48$  mPa s ( $\square$ ) and  $97$  mPa s ( $\circ$ ). (Courtesy of Ishino *et al* [39].)

$\alpha\ell/h_0$  and a time  $T = c\gamma\alpha^2t/\mu h_0$ , where  $c$  depends on the contact angle. In the case of conical tubes, the solution,  $L(T)$  is given by the polynomial solution

$$2L^4 + 8L^3 + 12L^2 = 3T, \quad (5)$$

which defines two distinct asymptotic limits:

At short times ( $T \ll 1$  or  $L \ll 1$ ), the meniscus is close to the cone's opening and the shape variation of the tube is not significant. In this limit, it is natural to recover the classical dynamics obtained with a capillary tube of constant cross section:  $L \propto T^{1/2}$ .

On the other hand, at long times ( $T \gg 1$ ), when the meniscus is far from the opening ( $L \gg 1$ ), the force balance is modified and we obtain  $L \propto T^{1/4}$ . To understand this difference, we note that first, the viscous dissipation is localized in the thinnest region of the cone, i.e. the tip. Second, the pressure drop at the meniscus, which is responsible for the movement, decreases when the cross section of the tube increases. Finally, mass conservation between the opening of the tube and the meniscus leads to a slowing down of the motion. The combination of these three effects gives different power-law responses, with exponents uniquely connected to the details of the geometry.

### 3.3. Dynamics of wicking within forests of micropillars (complete wetting)

Micropatterned surfaces have been extensively studied, both as model systems to understand generic effects of topographic or chemical heterogeneities on capillarity and wetting phenomena, but also from a material engineering perspective as means to obtain specific wetting or hydrodynamic effects. Examples include the creation of ultrahydrophobic surfaces [32, 33], the design of superoleophobic surfaces [34, 35], the possibility to generate tunable wetting by using an electric field [36], and the study of slip in the presence of surface heterogeneities [37, 38].

Here, we consider a microtextured surface brought into contact with a bath of completely wetting liquid (in the experiments, often silicone oil is used): the liquid spontaneously invades the microtexture as it would invade a capillary tube. In the case of a forest of micropillars, the film propagates by matching its thickness to the height of the posts. As previously mentioned, its progression follows the classical dynamics generally observed in porous media, i.e. the position of the front increases as the square root of time:  $\ell = \sqrt{Dt}$ .

Ishino *et al* correlate the dependence of the coefficient  $D$  with the geometric characteristics of the microtextures [39] (see figure 12(a)). The authors showed that the rougher

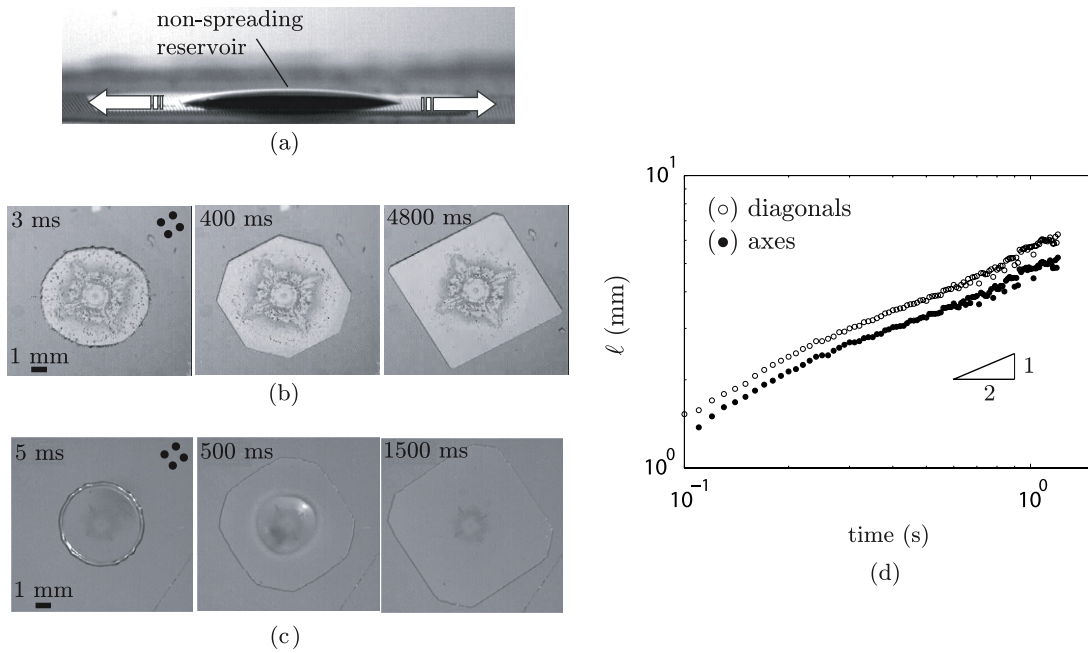


**Figure 13.** (a) Side view of a partially wetting fluid droplet on a microdecorated surface. As indicated by the arrows, spreading occurs by imbibition of the texture with a non-spreading macroscopic reservoir. The lattice parameters are  $d = 100 \mu\text{m}$ ,  $R = 25 \mu\text{m}$  and  $H = 30 \mu\text{m}$ . (b) When deposited on the surface, the drop rapidly adopts an initial circular shape ( $\sim 4 \text{ ms}$ ) followed by a transient octagon ( $\sim 400 \text{ ms}$ ) and a final square shape ( $\sim 4800 \text{ ms}$ ). (c) Time dependent spreading of a droplet on a microdecorated surface with identical lattice distance and posts radii as in (a) but larger height:  $d = 100 \mu\text{m}$ ,  $R = 25 \mu\text{m}$  and  $H = 60 \mu\text{m}$ . In contrast with the experiment in (b), the transient octagon ( $\sim 500 \text{ ms}$ ) does not transform into a square but remains octagonal at the end of spreading ( $\sim 1500 \text{ ms}$ ). The origin of time corresponds to the impact of the drop on the surface. (d) Evolution of the distance to the reservoir,  $\ell$ , as a function of time. This set of data correspond to the experiments shown in (b). Shown are the mean value of  $\ell$  along the four facets moving along the diagonals (O) and the axes (●). The ratio of the velocities along the diagonals and the axes is  $U_{\text{di}}/U_{\text{ax}} \approx 1.3$ . Figure adapted from [44].

the surface, the larger is the driving capillary force. Thus, increasing the pillar height or diameter, or decreasing the distance between the pillars, contributes to increasing the capillary suction. Meanwhile, the resistance comes from the viscous stresses that accompany flow. One contribution comes from gradients of velocity established over the height of the pillars, corresponding to viscous effects between the moving liquid and the bottom solid surface. For a given imbibition speed, the smaller the pillar height, the larger is the resulting viscous stress. In addition, the liquid flows into the forest of micropillars and viscous effects occur on their sides: in this case, the viscous force is essentially proportional to the height of the pillars and inversely proportional to the square of the lattice distance.

Thus, Ishino *et al* found that two different limits characterize the dynamics of wicking. For short pillars (of height smaller than the lattice spacing), the dominant viscous effect arises from the bottom solid surface. Therefore the larger the post, the faster the front progresses. In the other limit, for relatively tall pillars (of height bigger than the lattice distance), the viscous force is dominated by the dissipation on the pillar side so that the resulting imbibition coefficient  $D$  is independent of the pillar height and is mainly determined by the pillar radius. This analysis is confirmed by experiments realized on well-defined microtextures (figure 12) and illustrates that the dynamics of wicking can be tuned precisely by adjusting the texture geometry.

In this section, we have discussed cases of one-dimensional viscous imbibition in a tube or within a

microtexture. In this latter situation, the imbibition can occur along the different lattice directions that define the texture. We now discuss this situation in the case of partial wetting.

#### 4. Two-dimensional viscous imbibition

As presented in section 3, one-dimensional viscous imbibition is observed when a completely wetting fluid makes contact with a microtextured surface. Chemical patterning is often used to control two-dimensional wetting dynamics as seen in section 2. In particular, the literature documents ways of using surface chemistry to control the position, the size, and shape of drops on substrates [40–42]. Here we illustrate an example of directionally dependent imbibition of partially wetting on microtextured surfaces. As discussed in another contribution to this special issue on wetting, anisotropic spreading of partially wetting fluids can be obtained by changing the shape of the posts into triangles [43]. We next summarize our observations of polygonal footprints and ideas for shape selection during the spreading of a drop [44].

##### 4.1. Partial wetting of rough substrates

We used the square lattices shown in figure 1(c), and utilized different liquid that were partially wetting smooth surfaces made of the same material, with contact angles  $10^\circ < \theta_{\text{eq}} < 35^\circ$ . For partially wetting fluids, spreading occurs by imbibition of the roughness with a non-spreading reservoir (figure 13(a)). Perhaps surprisingly, it is possible that the

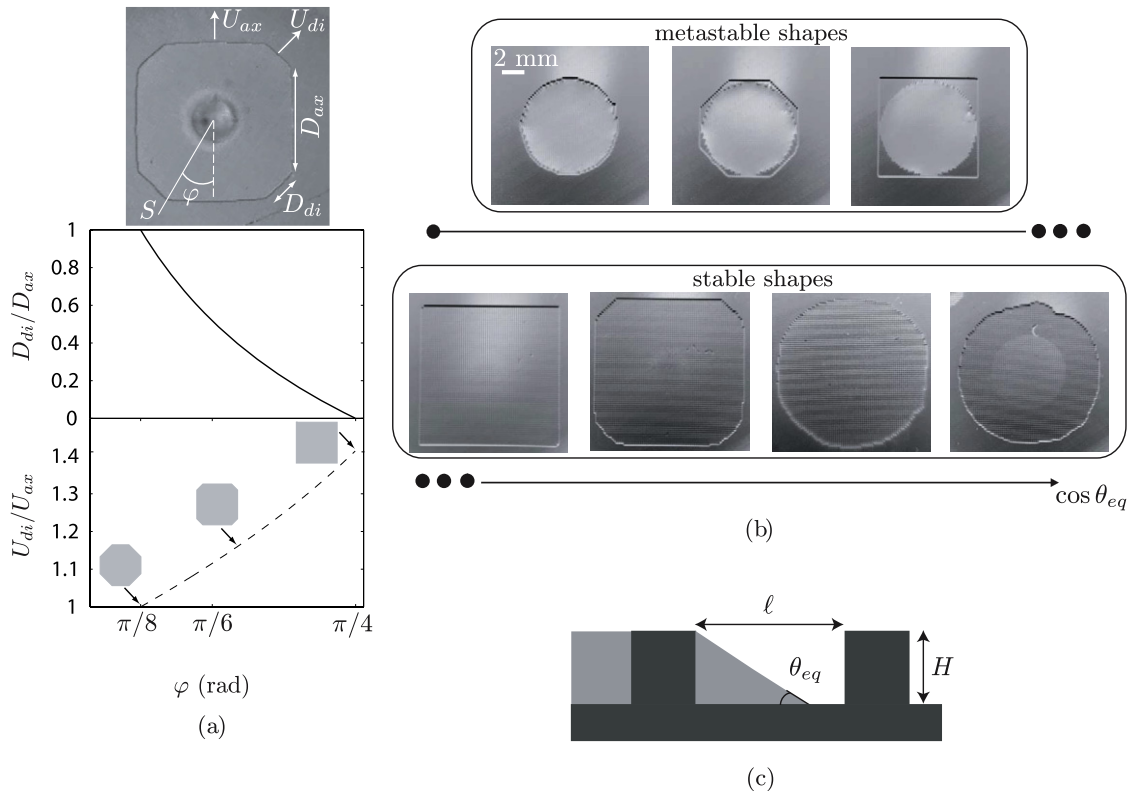


**Figure 14.** (a) Evolution of the facets sizes ratio  $D_{di}/D_{ax}$  and velocities ratio  $U_{di}/U_{ax}$  as a function of the angle  $\varphi$ . The dashed line corresponds to  $U_{ax}/\cos \varphi = U_{di}/\cos(\pi/4 - \varphi)$ . Inset: top view of an isopropanol droplet spreading on a surface roughness defining the variables  $U_{di}$ ,  $U_{ax}$ ,  $D_{di}$ ,  $D_{ax}$ , and  $\varphi$ . (b) Top view of the seven scenario for spreading of partially wetting fluids on a given rough surface. These seven final shapes are obtained by changing the wettability of the substrate, i.e.  $\cos \theta_{eq}$  with  $10^\circ < \theta_{eq} < 35^\circ$ . The lattice parameters are:  $d = 200 \mu\text{m}$ ,  $R = 50 \mu\text{m}$  and  $H = 50 \mu\text{m}$ . (c) Pinning of a contact line between two rows of posts (inter-post distance  $\ell$  and post height  $H$ ) with an equilibrium contact angle  $\theta_{eq}$ . Figure adapted from [44].

footprint of the wetting is no longer a circle. Rather, as we depict in figure 13(b) the transient spreading of a droplet, starts from an initial circle, passes through an intermediate octagon, and finally ends up with an equilibrium square shape. Two drops of the same partially wetting fluid deposited on surfaces with identical symmetries, post radii and lattice distances but different posts heights form different final shapes: a transient spreading octagon can either become a stable square (figure 13(b)) or remain an octagon as spreading ends (see figure 13(c)). Hence, we see that the shape selection depends on both the topographic features and the liquid through its equilibrium contact angle.

To explain the shape selection on microdecorated surfaces, it is crucial to understand the dynamics of spreading. We present in figure 13(d) the variations of  $\ell$ , the distance from the moving contact line to the reservoir as a function of time. Our experiments show that  $\ell \propto \sqrt{t}$  in both directions of the lattice. The results show that the prefactor in this spreading law is larger for movements along the diagonal. Similarly to the case of one-dimensional viscous wetting (see section 3), the dynamics of the imbibition of the texture by partially wetting fluids can be explained using Darcy's law [44].

The prefactor in the evolution of the contact line velocity,  $U$ , is a dimensionless function of the geometrical features that depends on the direction of the lattice; hence, differences can

be observed in the velocities along the diagonals and the axes,  $U_{di}$  and  $U_{ax}$ , as obtained in our experiments (in figure 13(d), we find  $U_{di}/U_{ax} \approx 1.3$ ).

The selection of a final shape (octagon or square) from a transient octagon depends of the velocity ratio  $U_{di}/U_{ax}$ . In order to obtain asymptotically stable shapes, the projections of  $U_{di}$  and  $U_{ax}$  on the line  $S$  that separates two sides of the transient octagon must be equal (see the definition of the variables in figure 14(a)). This condition is satisfied when  $U_{ax}/\cos \varphi = U_{di}/\cos(\pi/4 - \varphi)$ , where  $\varphi$  is the angle between the two facets. Our experiments show that  $U_{di} > U_{ax}$  which implies that  $\varphi \in [\pi/8, \pi/4]$ . Figure 14(a) shows the dependence on  $\varphi$  of both  $U_{di}/U_{ax}$  and of the facets size ratio  $D_{di}/D_{ax}$ . When  $U_{di}/U_{ax} = \sqrt{2}$ , i.e.  $\varphi = \pi/4$ , the axes facets grow slowly compared to the diagonal facets which shrink quickly. As a consequence, the final shape is a square,  $D_{di}/D_{ax} = 0$ . In contrast, octagons can be obtained for  $U_{di}/U_{ax} < \sqrt{2}$ . A regular octagon,  $D_{di}/D_{ax} = 1$ , can be observed only when  $U_{di}/U_{ax} = 1$ , i.e.  $\varphi = \pi/8$  (figure 14(a)).

We next release drops of the same size on a given microdecorated surface and vary the equilibrium contact angle,  $\theta_{eq}$ . We find five other macroscopic scenarios for wetting microdecorated surfaces as  $\cos \theta_{eq}$  is increased (figure 14(b)). The observed shapes can be organized into two distinct groups: three metastable shapes and four stable wetted domains. For

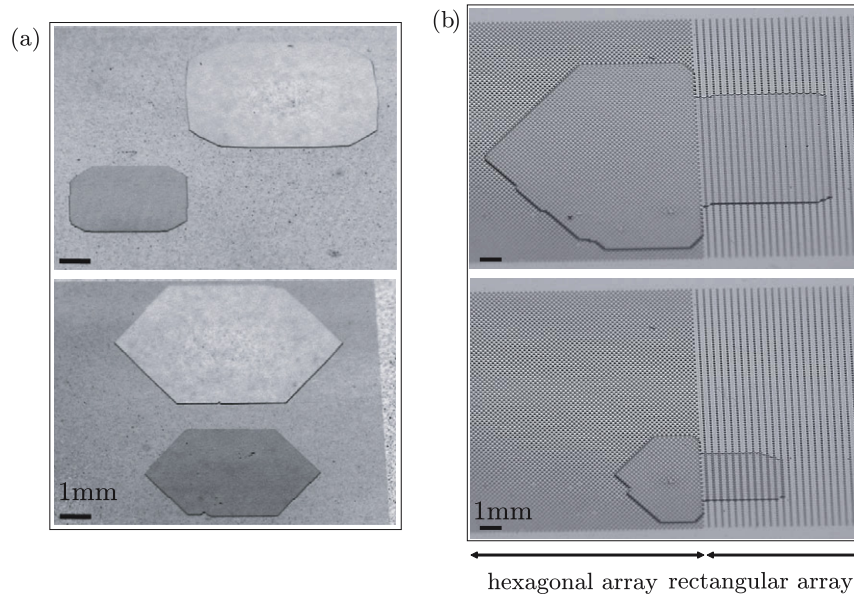


**Figure 15.** (a) Drops deposited on the same micropattern form the same shapes of different sizes when different volumes are used. Images were taken obliquely at an angle of about  $45^\circ$ . The liquid is isopropanol. (b) Photograph of the final shape (an arrow) obtained after deposition of a millimeter-size droplet at the boundary between two distinct patterns (a hexagonal and a rectangular lattice) on the substrate. An arrow of smaller size is obtained when the volume of the drop is decreased. In (a),  $d = 100 \mu\text{m}$ ,  $R = 25 \mu\text{m}$  and  $H = 60 \mu\text{m}$ . In (b), the parameters are  $d = 200 \mu\text{m}$ ,  $R = 50 \mu\text{m}$  and  $H = 50 \mu\text{m}$  for the hexagonal array, and  $R = 50 \mu\text{m}$ ,  $H = 50 \mu\text{m}$ ,  $d = 300 \mu\text{m}$  in the direction of the arrow and  $d = 200 \mu\text{m}$  perpendicularly to this direction for the rectangular lattice.

the first three, the contact line gets pinned in a well-defined metastable shape, either a circle, an octagon, or a square while the reservoir remains of finite size. In the four other scenarios, imbibition empties the reservoir and leaves a stable wetted domain: a square, an octagon, a rounded octagon, or a circle in the case of complete wetting, i.e. for  $\theta_{\text{eq}} = 0^\circ$  (for more details about the transition from faceted shapes to rounded octagons and circles, see [44]).

The transition from metastable to stable shapes can be understood by using simple energetic arguments [45]. Let us write the change in interfacial energy  $dE$  (per unit length of contact line) related to a small displacement  $dx$  of the liquid front invading the texture:  $dE = (\gamma_{sl} - \gamma_{sv})(r - \phi_s) dx + \gamma(1 - \phi_s) dx$ , where  $\phi_s$  and  $r$  are, respectively, the surface fraction of the top of the posts,  $\phi_s = \frac{\pi R^2}{d^2}$ , and the ratio of the true surface area to the projected one,  $r = 1 + \frac{2\pi RH}{d^2}$ . In this expression, the first and the second term are associated to the wetted domain and the creation of liquid/vapor interface. Imbibition should occur when energetically favorable,  $dE/dx < 0$ , or, in other words, when the equilibrium contact angle  $\theta_{\text{eq}}$  is lower than a critical angle  $\theta_{\text{eq}} < \theta_c$  with  $\cos \theta_c = \frac{1 - \phi_s}{r - \phi_s}$ . Using the roughness parameters of the substrate used in figure 14(b),  $\phi_s = 0.2$  and  $r = 1.4$ , we find  $\theta_c = 48^\circ$ . In our experiments,  $10^\circ < \theta_{\text{eq}} < 35^\circ$ . Therefore, even the fluid with the largest contact angle should imbibe the texture until the reservoir empties itself in the porosity and a thermodynamically stable shape is obtained. Our experiments, however, reveal the existence of a number of metastable shapes (see figure 14(b)). These shapes can be understood by considering the front meniscus at the scale of individual posts. In a first approximation, we consider that local pinning of the contact line can occur between two rows

of posts with a flat interface contacting the bottom surface with an angle  $\theta = \theta_{\text{eq}}$  (see figure 14(c)). This simple approach gives us a critical contact angle  $\theta_{\text{eq}} = \arctan(H/\ell)$  below which contact lines should get unpinned, the reservoir empties itself in the texture and a stable shape is formed. For the experiments shown in figure 14(b),  $H/\ell = 0.5$  gives a prediction of a critical angle  $\theta_{\text{eq}} = 27^\circ$  in very good agreement with the value we find experimentally: in figure 14(b), the transition from the circumscribed square to the stable square occurs for  $\theta_{\text{eq}} \simeq 27^\circ - 30^\circ$ .

Considerations of both the specificity of the lattice geometry and the dynamics of imbibition of the texture allow us to (i) understand the variety of metastable shapes and (ii) provide a ‘shape’ diagram that summarizes our results (see [44] for more details).

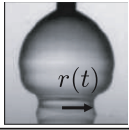
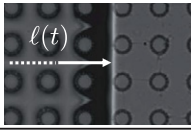
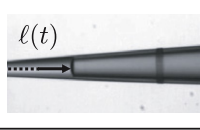
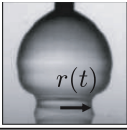


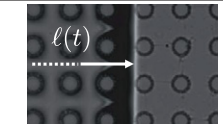
#### 4.2. Further investigations

Various polygonal shapes can be produced depending on the contact angle and the detailed topography of the surface pattern (e.g. the ratio of the height to spacing of the posts). In addition, as illustrated in figure 15(a), the footprint of a wetted shape is volume independent, which distinguishes these kinds of topographic wetted shapes from similar shapes obtainable with chemical patterning (e.g. [41]): the volume of a deposited drop controls the size of the final shape as shown in figure 15(a) for octagonal shapes formed on a square lattice and hexagons formed on a hexagonal lattice.

These observations form the starting point for new investigations. For example, the design of new geometries should be an efficient way to increase the number of realizable shapes. We illustrate this idea in figure 15(b). When a drop



**Table 1.** Conclusion tables that summarize our results and draw connections between our findings.

| Wetting   |   |   |   |
|---|---|---|---|
| Equilibrium contact angle   |   | Shape of the boundary   |   |
| inertial spreading<br> | viscous imbibition<br>   | viscous imbibition<br>  | inertial spreading<br> |
| $\theta_{eq} = 0^\circ$<br>$r \propto t^{1/2}$  | $\theta_{eq} = 0^\circ$<br> isotropic imbibition                           | imbibition in tubes<br>$\ell \propto t^{1/2}$   | spherical drops<br>( $\theta_{eq} = 0^\circ$ )<br>$r \propto t^{1/2}$                                     |
| $0^\circ < \theta_{eq} < 117^\circ$<br>$r \propto t^\alpha \quad \alpha = \frac{1}{4} - \frac{1}{2}$    | $10^\circ < \theta_{eq} < 35^\circ$<br> directionally dependent imbibition | imbibition in cones<br>$\ell \propto t^{1/2}$ at short times<br>$\ell \propto t^{1/4}$ at long times  | conical drops<br>( $\theta_{eq} = 0^\circ$ )<br>$r \propto t^{2/3}$                                       |
| (a)   |   | (b)   |   |
| Roughness of the surface texture  |   |   |   |
|                        |   | Diffusive imbibition, $\ell \propto t^{1/2}$ , describes the dynamics of one-dimensional and two-dimensional wicking of microtextured surfaces. |   |
| (c)   |   |   |   |

of partially wetting liquid is deposited at the boundary of two micropatterns of distinct geometries, new shapes can be produced. In the example shown in figure 15(b), a millimeter-size drop of isopropanol deposited at the boundary of a hexagonal lattice and a rectangular lattice of posts spreads over each of the two microtextures to form a final shape that resembles an arrow. As shown in this figure, this shape is independent of the volume delivered.

Although the scope of this paper focuses on the phenomenon of wetting, it is worthwhile mentioning that our observations also suggest that these experiments could be an efficient way to generate heterogeneous nucleation of gas microbubbles. Indeed, we observe upon impact of a drop with the surface anisotropic air trapping inside the surface texture: individual microbubbles get trapped between two posts (see figure 16). The assembly of microbubbles forms a domain whose shape strongly depends on the topographic and impact parameters. For example, microbubbles can form a cross-like structure or a shape resembling a four-leaf clover (in figure 16, the white spots are the microbubbles and the darker domains indicate the location of liquid on the substrate). Future investigations might explain how the size of the microbubbles and the shape of the domains depend on the impact parameters and the surface topography.

## 5. Conclusion

Here we have demonstrated variations in the dynamics of wetting for three distinct configurations: (i) spreading of drops (ii) imbibition by complete wetting fluids of one-dimensional

and two-dimensional porosities, and (iii) polygonal spreading by imbibition of partially wetting fluid on rough substrates. This research highlights the diversity of capillary-driven phenomena, while also noting parallels between these systems. We summarize these ideas in table 1. Specifically, we have shown that the equilibrium contact angle can influence both the spreading dynamics of drops and the shapes of imbibing fronts of fluids in microtextures. Similarly, wetting dynamics are influenced by the shape of interfacial boundary of spreading drops and the wall geometry of wetted tubes. Finally, our results show that diffusive imbibition can explain the wetting of tubes and cones (at short time of spreading), and the one-dimensional and two-dimensional wicking of microtextured substrates.

Adding complexity in the combination of changes in the shape of boundaries, equilibrium contact angle, and surface roughness, may simplify ways to control wetting dynamics in a variety of situation. Further investigations could combine some of these ideas such as the effect of change in equilibrium contact angle on the spreading of a conical drop. Finally, future work could expand the ideas of shapes and surface chemistries to other recently explored wetting configurations [46, 47].

## Acknowledgments

We are thankful to numerous colleagues for many helpful discussions. We especially thank A Ajdari, E Denieul, E Dressaire, C Ishino, S Mandre, K Okumura, D Quéré, E Reyssat, and M Roper for their contributions to the subjects treated here. We thank Harvard MRSEC (DMR-0820484) for



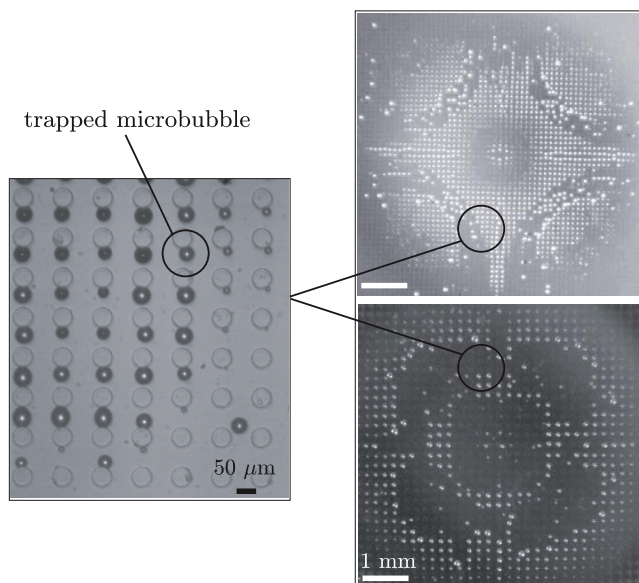


**Figure 16.** Left panel: close-up at the scale of individual posts showing individual microbubbles trapped between two posts. Right panel: different shapes formed by trapped microbubbles after impact of an ethanol droplet on microdecorated surfaces with the same symmetry (square) but different lattice parameters: (top picture)  $d = 100 \mu\text{m}$ ,  $R = 25 \mu\text{m}$  and  $H = 50 \mu\text{m}$  and (bottom picture)  $d = 200 \mu\text{m}$ ,  $R = 50 \mu\text{m}$  and  $H = 50 \mu\text{m}$ . The height of release of the drop is 50 cm. The white spots are the trapped microbubbles and the darker areas indicate the presence of the fluid on the surface.

support of this research. This work was performed in part at the Center for Nanoscale Systems (CNS), a member of the National Nanotechnology Infrastructure Network (NNIN), which is supported by the National Science Foundation under NSF award no. ECS-0335765. CNS is part of the Faculty of Arts and Sciences at Harvard University.

## References

- [1] Bouasse H 1924 *Capillarité-Phénomènes Superficiels* (Paris: Librairie Delagrave)
- [2] de Gennes P G 1985 *Rev. Mod. Phys.* **57** 827
- [3] de Gennes P G, Brochard-Wyart F and Quéré D 2004 *Capillarity and Wetting Phenomena: Drops, Bubbles, Pearls, Waves* (New York: Springer)
- [4] Bonn D, Eggers J, Indekeu J, Meunier J and Rolley E 2009 *Rev. Mod. Phys.* **81** 739
- [5] Courbin L and Stone H A 2007 *Phys. Today* **60** (2) 84
- [6] Quéré D 2005 *Rep. Prog. Phys.* **68** 2495
- [7] McDonald J C and Whitesides G M 2002 *Acc. Chem. Res.* **35** 491
- [8] Barthlot W and Neinhuis C 1997 *Planta* **202** 1
- [9] Bird J C, Mandre S and Stone H A 2008 *Phys. Rev. Lett.* **100** 234501
- [10] Biance A L, Clanet C and Quere D 2004 *Phys. Rev. E* **69** 016301
- [11] Tanner L H 1979 *J. Phys. D: Appl. Phys.* **12** 1473
- [12] Thoroddsen S T and Takehara K 2000 *Phys. Fluids* **12** 1265
- [13] Blanchette F and Bigioni T P 2006 *Nat. Phys.* **2** 254
- [14] Hardy W B 1919 *Phil. Mag.* **38** 32
- [15] Huh C and Scriven L E 1971 *J. Colloid Interface Sci.* **35** 85
- [16] Drelich J and Chibowska D 2005 *Langmuir* **21** 7733
- [17] Keller J B, Milewski P A and Vanden-Broeck J M 2000 *Eur. J. Mech. B* **19** 491
- [18] Billingham J and King A C 2005 *J. Fluid Mech.* **533** 193
- [19] Saville D A 1997 *Annu. Rev. Fluid Mech.* **29** 27
- [20] Melcher J R and Taylor G I 1969 *Annu. Rev. Fluid Mech.* **1** 111
- [21] Brazier-Smith P R 1971 *Phys. Fluids* **14** 1
- [22] Eggers J, Lister J R and Stone H A 1999 *J. Fluid Mech.* **401** 293
- [23] Quéré D 1997 *Europhys. Lett.* **39** 533
- [24] Chebbi R 2007 *J. Colloid Interface Sci.* **315** 255
- [25] Washburn E W 1921 *Phys. Rev.* **17** 273
- [26] Lucas V R 1918 *Kolloid Z.* **23** 15
- [27] Bell J M and Cameron F K 1906 *J. Phys. Chem.* **10** 658
- [28] Dullien F A L 1979 *Porous media Fluid Transport and Pore Structure* (New York: Academic)
- [29] Romero L A and Yost F G 1996 *J. Fluid Mech.* **322** 109
- [30] Rye R R, Yost F G and O'Toole E J 1998 *Langmuir* **14** 3937
- [31] Reyssat M, Courbin L, Reyssat E and Stone H A 2008 *J. Fluid Mech.* **615** 335–44
- [32] Onda T, Shibuichi N, Satoh N and Tsuji K 1996 *Langmuir* **12** 2125
- [33] Quéré D 2002 *Nat. Mater.* **1** 14
- [34] Tuteja A, Choi W, Ma M, Mabry J M, Mazzella S A, Rutledge G C, McKinley G H and Cohen R E 2007 *Science* **318** 1618
- [35] Ahuja A, Taylor J A, Lifton V, Sidorenko A A, Salamon T R, Lobaton E J, Kolodner P and Krupenkin T N 2008 *Langmuir* **24** 9
- [36] Krupenkin T N, Taylor J A, Schneider T M and Yang S 2004 *Langmuir* **20** 3824
- [37] Cottin-Bizonne C, Barrat J L, Bocquet L and Charlaix E 2003 *Nat. Mater.* **2** 237
- [38] Lauga E and Stone H A 2003 *J. Fluid Mech.* **489** 55
- [39] Ishino C, Reyssat M, Reyssat E, Okumura K and Quéré D 2007 *Eur. Phys. Lett.* **79** 56005
- [40] Cubaud T and Fermigier M 2001 *Europhys. Lett.* **55** 239
- [41] Abbott N L, Folkers J P and Whitesides G M 1992 *Science* **257** 1380
- [42] Gau H, Herminghaus S, Lenz P and Lipowski R 1999 *Science* **283** 46
- [43] Blow M L, Kusumaatmaja H and Yeomans J M 2009 *J. Phys.: Condens. Matter* **21** 464125
- [44] Courbin L, Denieul E, Dressaire E, Roper M, Ajdari A and Stone H A 2007 *Nat. Mater.* **6** 661
- [45] Bico J, Tordeux C and Quéré D 2001 *Europhys. Lett.* **55** 214
- [46] Quéré D 1997 *Europhys. Lett.* **39** 533
- [47] Aarts D G A L, Lekkerkerker H N W, Guo H, Wegdam G H and Bonn D 2005 *Phys. Rev. Lett.* **95** 164503